ARMY RESEARCH LABORATORY

Lamb Wave Polarization Techniques for Structural Damage Localization and Quantification

by James T. Ayers, Eric Swenson, C. Todd Owens, Massimo Ruzzene, Anindya Ghoshal, and Dy D. Le

ARL-TR-5817 **November 2011**

NOTICES

Disclaimers

The findings in this report are not to be construed as an official Department of the Army position unless so designated by other authorized documents.

Citation of manufacturer's or trade names does not constitute an official endorsement or approval of the use thereof.

Destroy this report when it is no longer needed. Do not return it to the originator.

Army Research Laboratory
Aberdeen Proving Ground, MD 21005-5069

ARL-TR-5817 **November 2011**

Lamb Wave Polarization Techniques for Structural Damage Localization and Quantification

James T. Ayers, Anindya Ghoshal, and Dy D. Le
Vehicle Technology Directorate, ARL

Eric Swenson and C. Todd Owens
Air Force Institute of Technology

Massimo Ruzzene
Georgia Institute of Technology

REPORT DOCUMENTATION PAGE	Form Approved OMB No. 0704-0188

1. REPORT DATE *(DD-MM-YYYY)*	2. REPORT TYPE	3. DATES COVERED (From - To)
November 2011	Final	January 2011–August 2011

4. TITLE AND SUBTITLE
Lamb Wave Polarization Techniques for Structural Damage Localization and Quantification

5a. CONTRACT NUMBER

5b. GRANT NUMBER

5c. PROGRAM ELEMENT NUMBER

6. AUTHOR(S)
James T. Ayers, Eric Swenson,[*] C. Todd Owens,[*] Massimo Ruzzene,[†]
Anindya Ghoshal, and Dy D. Le

5d. PROJECT NUMBER

5e. TASK NUMBER

5f. WORK UNIT NUMBER

7. PERFORMING ORGANIZATION NAME(S) AND ADDRESS(ES)
U.S. Army Research Laboratory
ATTN: RDRL-VTM
Aberdeen Proving Ground, MD 21005-5069

8. PERFORMING ORGANIZATION REPORT NUMBER
ARL-TR-5817

9. SPONSORING/MONITORING AGENCY NAME(S) AND ADDRESS(ES)

10. SPONSOR/MONITOR'S ACRONYM(S)

11. SPONSOR/MONITOR'S REPORT NUMBER(S)

12. DISTRIBUTION/AVAILABILITY STATEMENT
Approved for public release; distribution is unlimited.

13. SUPPLEMENTARY NOTES
[*]Air Force Institute of Technology, Wright-Patterson Air Force Base, Dayton, OH
[†]Georgia Institute of Technology, Atlanta, GA

14. ABSTRACT
U.S. Army rotorcraft and land-based vehicles develop induced structural damage that requires robust damage diagnostics that characterize these real-time defects. This report investigates one such method based on polarization of guided waves. Initially, an analytical description of polarized Lamb wave components that yield an elliptical, rotated profile of the particle trajectory is provided. A damage localization technique is shown to utilize the elliptical orientation as a damage identification parameter for guided wave structural interrogation techniques. In addition, a damage quantification technique incorporates spatially integrated multiple component mode coefficients that are formulated in the frequency-spatial domain with the intent to better characterize wave reflections and mode conversions. The techniques are applied to finite-element (FE) models of aluminum and composite armor-like structures. Trends from the two-dimensional FE numerical studies are verified by a three-dimensional scanning laser vibrometry test setup for the undamaged case. Recommendations of implementing the polarization techniques for damage localization and quantification on Army platforms are given.

15. SUBJECT TERMS
structural health monitoring, Lamb waves, damage localization, polarization, quantification

16. SECURITY CLASSIFICATION OF:			17. LIMITATION OF ABSTRACT	18. NUMBER OF PAGES	19a. NAME OF RESPONSIBLE PERSON
a. REPORT	b. ABSTRACT	c. THIS PAGE			James T. Ayers
Unclassified	Unclassified	Unclassified	UU	26	19b. TELEPHONE NUMBER (*Include area code*) 410-278-7650

Standard Form 298 (Rev. 8/98)
Prescribed by ANSI Std. Z39.18

Contents

List of Figures

List of Tables

INTENTIONALLY LEFT BLANK.

1. Introduction

Polarization defines the phase and amplitude relationships between the various components of wave motion and is significant in all technological applications based on wave propagation, such as optics, seismology, telecommunications, and radar science. As opposed to other fields, elastic wave polarization within the U.S. Army has received relatively little attention due to the general difficulty in evaluating it experimentally. It is, however, a well-recognized fact that the ability to measure and characterize the polarization of ultrasonic elastic waves could lead to the development of novel structural diagnostic tools, which could rely on the sensitivity of polarization to surface roughness, cracks, temperature, or residual stresses, among others.

The theoretical study of the polarization of Rayleigh surface waves presented in Miklowitz (*1*) suggests its estimation as an alternative method for surface stress estimation. A polarization parameter can be defined as the ratio between the maximum in-plane and out-of-plane displacement components and can be directly related to the state of surface stress and thus be used as an absolute measurement of pre-stress. Studies on the acousto-elastic effect on Rayleigh waves in a homogeneous material include the work of Hirao et al. (*2*) and Duquennoy et al. (*3*). The analysis of polarization of ultrasonic guided waves is even more limited and has mostly focused on theoretical aspects related to the description of the wavefield and to tuning criteria for the excitation of specific wave modes through surface-mounted transducers (*4*–*6*). Recent work by the present authors has shown the experimental validation of the polarized components using one-dimensional scanning laser Doppler vibrometry (SLDV) for Rayleigh waves (*7*) and extended to Lamb waves to quantify damage in metallic plates (*8*, *9*).

One specific component that has direct Army significance is the stiffener-plate configuration, or so-called T-joint, which is ubiquitous in aerospace components and most commonly represented in the wing airfoil-spar and bulkhead-stiffener interfaces found in Army rotorcraft. A nominal fillet is generally designed at the interface to alleviate potential stress concentrations, which can produce initiatory cracks under high-cycle loading conditions. However, these T-joint configurations provide a challenge for structural health monitoring (SHM) strategies that employ wave propagation-based interrogation techniques such that partial transmission, reflection, and mode conversion are modified by the degree of the fillet radius, excitation frequency, material constituency, and stiffener cross-sectional thickness (*10*). Since the success of this proposed SHM strategy to assess damage severity largely depends on the quantification of the mode conversion, a fundamental understanding of the wave interaction due to the T-joint presence is necessary.

Previous work has been conducted on understanding T-joint configurations of various material constituencies and a range of damage quantification techniques. Modal techniques employed by Ooijevaar et al. (*11*) and Sundaresan et al. (*12*) used scanning laser vibrometry to detect damage

produced in composite plate with two T-shaped stiffener sections and induced long saw cuts on an aluminum wing panel, respectively. In terms of wave propagation techniques, Greve et al. (*13*) analyzed Lamb wave interactions of a cracked welded joint and rolled and plate girders using two-dimensional (2-D) and three-dimensional (3-D) finite element modeling (FEM). Simulations and experiments showed cracks that are oriented perpendicular to the direction of wave propagation cause strong reflections. Oppenheim et al. (*10*) modeled a 2-D simulation of Lamb wave transmission/reflection at a T-joint with no fillet radius using Abaqus* and a 3-D model of a plate girder. Experimental measurements using piezoelectric (PZT) sensors were located on the web in pulse-echo mode, and the response demonstrated dominant S_0 mode reflections. Similarly, Morvan et al. (*14*) measured Lamb waves by a laser vibrometer in a T-joint generated by a contact piezo-composite transducer and normal component of the surface wave displacement of the plate and stiffener. Kim et al. (*15*) analyzed mode conversion of T-joint with collocated PZT sensors before and after the stiffener using a 2-D simulation under plane strain assumptions. Other studies concluded, with experimental evidence, that damage-sensitive features are successfully extracted as damage-induced Lamb wave modes have unique characteristics compared to those modes produced by the stiffener or varying thickness (*16*, *17*).

The initial aim of this report is to investigate whether the polarization nature of Lamb waves may be utilized as a damage localization technique. Specifically, an analytical formulation of the Lamb wave elliptical trajectory orientation is developed. Based on the formulation, two simplified damage localization parameters are proposed, and finite simulations demonstrate their potential use. The techniques are then applied to metallic and composite plates at varying excitation frequencies with different geometries and damage type, and a 3-D SLDV setup is implemented to extract the orthogonal displacement components. The primary advantage of the techniques is shown to reduce the required signal processing while enabling high-resolution damage localization. A secondary objective of this report is to further understand the mode conversion mechanism at the T-joint interface using frequency-wave number filtering techniques per Ruzzene (*18*), both as a function of the fillet radius with and without blind-side damage and with experimental validation that provides high-fidelity spatial resolution using 3-D laser vibrometry.

2. Analytical Lamb Wave Polarization Formulation

The particle trajectory at a given location is calculated based on the analytical Lamb wave model provided by Raghavan et al. (*19*). For the given formulation, the displacement is initially described as a superposition of the fundamental symmetric (S) and anti-symmetric (A) Lamb wave modes at a frequency lower than the first anti-symmetric mode cutoff. The far field approximations are used and written in the following compact form (*1*):

*ABAQUS is a registered trademark of ABAQUS, Inc.

$$u_1(r,\omega) = A_1^S e^{i(\varphi_S - \pi/2)} + A_1^A e^{i(\varphi_A - \pi/2)}\,, \tag{1}$$

and

$$u_3(r,\omega) = A_3^S e^{i\varphi_S} + A_3^A e^{i\varphi_A}\,, \tag{2}$$

where

$$\varphi_S = -k_S r + \frac{\pi}{4}\,,\ \varphi_A = -k_A r + \frac{\pi}{4}\,, \tag{3}$$

such that u_1 and u_3 are the in-plane and out-of-plane displacements, r is the radial distance away from the piezoelectric source, ω is the frequency, A is the amplitude of the respective displacement component and mode, and k is the wave number. Normalization of the displacements by

$$\bar{u}_j = \frac{Real(u_j)}{|u_3|} \quad (j = 1,3) \tag{4}$$

results in

$$\bar{u}_1 = \frac{A_1^S \sin(\varphi_S) + A_1^A \sin(\varphi_A)}{\sqrt{(A_3^S)^2 + (A_3^A)^2 + 2A_3^S A_3^A \cos(\varphi)}} \tag{5}$$

and

$$\bar{u}_3 = \frac{A_3^S \sin(\varphi_S) + A_3^A \sin(\varphi_A)}{\sqrt{(A_3^S)^2 + (A_3^A)^2 + 2A_3^S A_3^A \cos(\varphi)}}\,. \tag{6}$$

Using trigonometric identities within equations 5 and 6 leads to the following:

$$\bar{u}_1 = \frac{1}{\Gamma}(A_1^S \sin\varphi_S + A_1^A \sin\varphi_S \cos\varphi + A_1^A \cos\varphi_S \sin\varphi)\,, \tag{7}$$

and

$$\bar{u}_3 = \frac{1}{\Gamma}(A_3^S \cos\varphi_S + A_3^A \cos\varphi_S \cos\varphi - A_3^A \sin\varphi_S \sin\varphi)\,, \tag{8}$$

where

$$\Gamma = \sqrt{(A_3^S)^2 + (A_3^A)^2 + 2A_3^S A_3^A \cos\varphi}\ . \tag{9}$$

In matrix form, equations 7 and 8 are rewritten as follows:

$$\begin{Bmatrix} \bar{u}_1 \\ \bar{u}_3 \end{Bmatrix} = \begin{bmatrix} B_{11} & B_{12} \\ B_{21} & B_{22} \end{bmatrix} \begin{Bmatrix} \sin\varphi_S \\ \cos\varphi_S \end{Bmatrix}, \tag{10}$$

where

$$B_{11} = \frac{1}{\Gamma}(A_1^S + A_1^A \cos\varphi),\ B_{12} = \frac{1}{\Gamma}A_1^A \sin\varphi$$

and

$$B_{21} = -\frac{1}{\Gamma}A_3^A \sin\varphi\,,\ B_{22} = \frac{1}{\Gamma}(A_3^S + A_3^A \cos\varphi)\,. \tag{11}$$

Solving the matrix in equation 10 results in the following:

$$\sin\varphi_S = \frac{1}{\mathrm{B}}(\bar{u}_1 B_{22} - \bar{u}_3 B_{12})\,, \tag{12}$$

and

$$\cos\varphi_S = \frac{1}{\mathrm{B}}(-\bar{u}_1 B_{21} + \bar{u}_3 B_{11})\,, \tag{13}$$

where $B = B_{11}B_{22} - B_{12}B_{21}$. Squaring and summing equations 12 and 13 produces

$$\frac{1}{B^2}[(\bar{u}_1 B_{22} - \bar{u}_3 B_{12})^2 + (-\bar{u}_1 B_{21} + \bar{u}_3 B_{11})^2] = 1\,. \tag{14}$$

Upon assigning the following parameters,

$$a = \frac{B}{\sqrt{B_{22}^2 + B_{12}^2}}\,, \tag{15}$$

$$b = \frac{B}{\sqrt{B_{11}^2 + B_{21}^2}}\,, \tag{16}$$

and

$$\cos\Omega = \frac{B_{22}}{\sqrt{B_{22}^2 + B_{12}^2}}\,. \tag{17}$$

Applying equations 15–17 to equation 14 results in a rotated elliptical equation (figure 1) as follows:

$$(\bar{u}_1 \frac{\cos\Omega}{a} - \bar{u}_3 \frac{\sin\Omega}{a})^2 + (\bar{u}_1 \frac{\sin\Omega}{b} + \bar{u}_3 \frac{\cos\Omega}{b})^2 = 1\,. \tag{18}$$

Physically, it can be shown that the representation of the polarized components of the guided waves, $\bar{u}_1$ and $\bar{u}_3$, yield an elliptical, rotated profile of the particle trajectory.

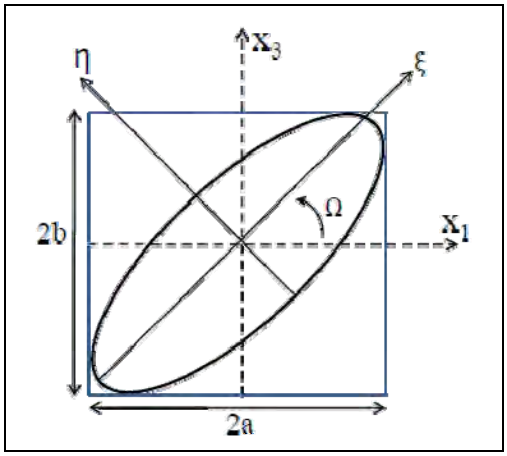

Figure 1. Lamb wave elliptical trajectory profile with identified parameters.

Figure 2a illustrates the Lamb wave polarization ellipses as a function of *r*, the radial distance away from the piezoelectric source. Figure 2b shows the projections of these ellipses in ($\bar{u}_1$, r) plane.

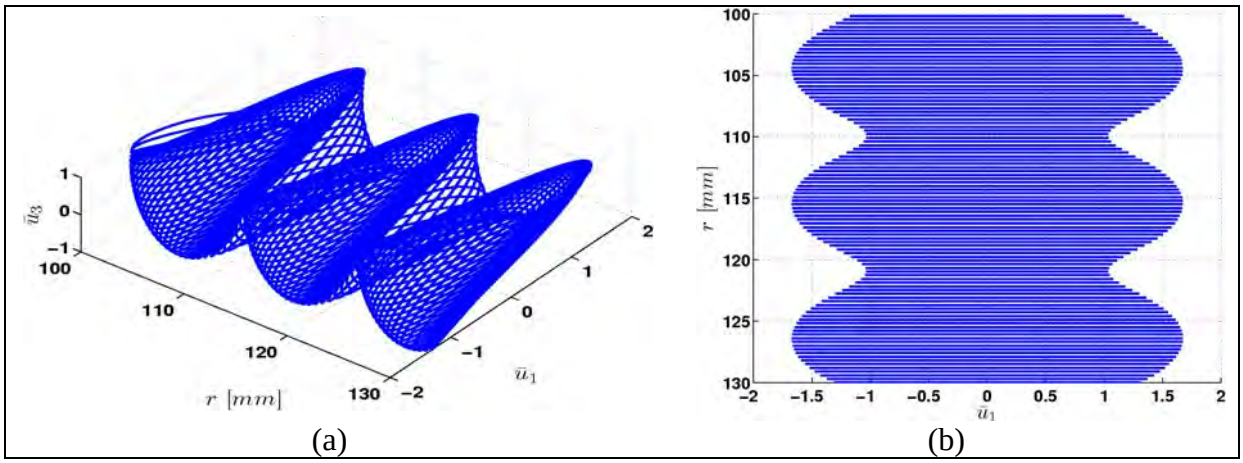

Figure 2. Image showing (a) normalized elliptical trajectory as function of the distance away from the source and (b) planform view of the in-plane polarized component as function of the distance away from the source.

2.1 Damage Localization

Two damage localization parameters based on the elliptical trajectory orientation (ETO) are proposed. The first is based on the observation that the period of the orientation (when shown as a function of the distance of the piezoelectric actuator) varies in relationship to the period of the incident wave. The localization parameter, denoted as Π_{ETO}, may be formulated as a ratio of the resulting period, Ω_j, and the incident period such that:

$$\Pi_{\mathrm{ETO}}(\Delta r, \omega) = \frac{T_{\Omega_j}(\Delta r,\omega)}{T_{\Omega_i}(\Delta r,\omega)}, \tag{19}$$

where *T* is the period of the elliptical orientation as function of *r* and subscripts *i* and *j* are incident and resulting periods, respectively. The parameter is a function of Δr as a result of the period calculated from the orientation changing over the radial. This formulation has the distinct advantage of relying on time domain spatial-temporal response and thereby eliminates the domain signal processing that previous damage localization parameters have commonly employed (*20*).

A second proposed damage indicator, denoted for convenience as Ψ_{ETO}, is based on the amplitude differential of the periodic elliptical orientation, δ_i, as a function of the distance away from the source such that

$$\delta_i(\Delta r, \omega) = \Omega_{i+1} - \Omega_i \tag{20}$$

and

$$\Psi_{\mathrm{ETO}}(\Delta r,\omega)=\frac{\delta_i}{\max\left(\delta_i\right)}\ , \tag{21}$$

where the Ψ_{ETO} parameter is normalized by the maximum periodic amplitude differential.

2.2 Damage Quantification

This analysis is restricted to the frequency range of the fundamental symmetric and antisymmetric Lamb waves, S_0 and A_0, respectively. As illustrated in figure 3, it is assumed that a pure S_0 or A_0 mode is generated to interrogate the structure. The interaction of an incident S_0 mode with a vertical stiffener causes a partial S_0 reflection and partial mode conversion into the A_0 mode while simultaneously producing a partial S_0 and A_0 mode transmission into the stiffener and the plate. As previously described by Ayers et al. (*21*), upon filtering the data in the frequency-wave number domain and windowing the data in the time-space domain, $\widetilde{w}(x,\omega)$ is the filtered response in the spatial-frequency domain of a single extracted mode at frequency ω.

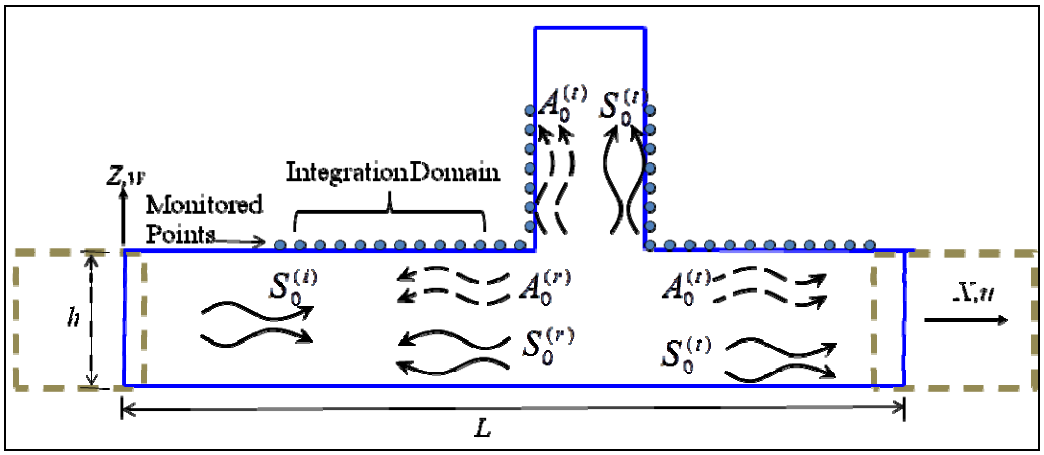

Figure 3. Schematic of T-joint and mode conversion identification.

Laser vibrometry techniques allow for various points to be scanned over the distance, L. From the measured responses, the value of the mode coefficients may be estimated over a spatial domain. This allows the estimation of its spatial-independence and more importantly of a spatially averaged value, which is less affected by amplitude fluctuations due to noise or by general trends associated with geometrical spreading. In compact matrix notation, the mode coefficients may be expressed by the following for an interrogating S_0 mode but are likewise easily applied for an interrogating A_0 mode as follows:

$$\Pi_{ij}(w)=\frac{\int_{\Omega_{1j}}^{\Omega_{2j}}\left|\psi_{ij}(x,\omega)\right|dx}{\int_{x_1}^{x_2}\left|\Phi_i(x,\omega)\right|dx}\ , \tag{22}$$

where

$$\Pi_{ij}(w) = \begin{bmatrix} R^{u}_{S_0} & T^{u}_{S_0} & C^{u}_{A_0} \\ R^{w}_{S_0} & T^{w}_{S_0} & C^{w}_{A_0} \\ R^{uw}_{S_0} & T^{uw}_{S_0} & C^{uw}_{S_0} \end{bmatrix}, \tag{23}$$

$$\Psi_{ij}(w) = \begin{bmatrix} \dfrac{\tilde{u}^{(r)}_{S_0}}{\sqrt{(\tilde{u}^{(r)}_{S_0})^2 + (\tilde{w}^{(r)}_{S_0})^2}} & \dfrac{\tilde{u}^{(t)}_{S_0}}{\sqrt{(\tilde{u}^{(t)}_{S_0})^2 + (\tilde{w}^{(t)}_{S_0})^2}} & \dfrac{\tilde{u}^{(r)}_{A_0}}{\sqrt{(\tilde{u}^{(r)}_{A_0})^2 + (\tilde{w}^{(r)}_{A_0})^2}} \\ \dfrac{\tilde{w}^{(r)}_{S_0}}{\sqrt{(\tilde{u}^{(r)}_{S_0})^2 + (\tilde{w}^{(r)}_{S_0})^2}} & \dfrac{\tilde{w}^{(t)}_{S_0}}{\sqrt{(\tilde{u}^{(t)}_{S_0})^2 + (\tilde{w}^{(t)}_{S_0})^2}} & \dfrac{\tilde{w}^{(r)}_{A_0}}{\sqrt{(\tilde{u}^{(r)}_{A_0})^2 + (\tilde{w}^{(r)}_{A_0})^2}} \end{bmatrix}, \tag{24}$$

and

$$\Phi_{i}(w) = \begin{bmatrix} \tilde{u}^{(i)}_{S_0} & \tilde{w}^{(i)}_{S_0} & \sqrt{(\tilde{u}^{(i)}_{S_0})^2 + (\tilde{w}^{(i)}_{S_0})^2} \end{bmatrix}, \tag{25}$$

and

$$\Omega_{ij}(x) = \begin{bmatrix} x_1 & x_3 & x_1 \\ x_2 & x_4 & x_2 \end{bmatrix}, \tag{26}$$

where *R*, *T*, and *C* parameters represent the reflection, transmission, and converted coefficients, *u* and *w* are the in-plane and out-of-plane displacement components, respectively, and x_i values are the integration spatial coordinates. It is important to note that this spatial integration method departs from existing literature, where the mode amplitudes are taken at a fixed location (*21*).

3. Numerical Results

3.1 Damage Localization

A simplified plane strain finite element model is employed to evaluate the feasibility of the damage localization parameters. Specifically, an isotropic, homogeneous plate with varying notch types at the mid-span is developed using the commercial software Abaqus. The plate dimensions are 2×10^{-3} m in height, 5×10^{-1} m in width, and 1.0 m in length. The material properties reflect those of nominal Al 7075-T6, where the density $\rho = 2800$ kg/m^3, elastic modulus E = 72 GPa, and Poisson's ratio $\nu = 0.33$. A longitudinal uniform pressure tip load is applied at one end of the plate, whereas the opposite end is fixed. The symmetry of the applied in-plane load ensures that only the S_0 mode is excited, which is later verified in the frequency-wave number domain during data post-processing. The equations of motion are solved by the explicit central-difference time integration rule, which is suitable for large models with short dynamic response. The central-difference operator is conditionally stable, and in order to have an accurate solution, the integration time step Δt is chosen such that $\Delta t = f_0/20$, where f_0 is the highest frequency of interest, measured in Hz (*22*).

For a given excitation of 200 kHz in figure 4a, the incident period over the radial distance from 0 to 0.2 m is 0.013 m (figure 4b), which includes the incident and reflected fundamental symmetric modes. In contrast, from figure 4b, the resulting period over the (0.2–0.5-m) radial distance is 0.06 m, which is the summation of the incident and reflected fundamental symmetric mode, S_0, and an additional converted antisymmetric mode, A_0. Applying equation 19, the consequent Π_{ETO} is shown in figure 5, where the amplitude is unity except at the periodic discontinuities at r = 0.2, 0.5, and 0.8 m. These discrete periodic discontinuities indicate the presence of mode conversion and consequent damage localization without additional domain signal processing algorithms.

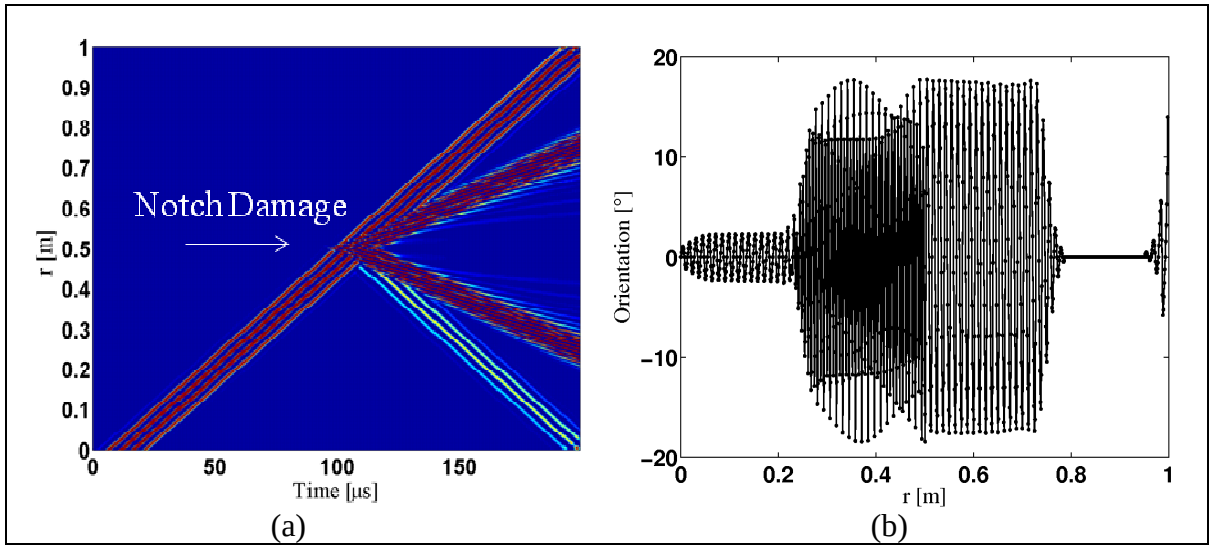

Figure 4. Image showing (a) in-plane spatial-temporal domain of surface response with indicated notch damage location at r = 0.5 m and (b) elliptical trajectory orientation as a function of radial distance.

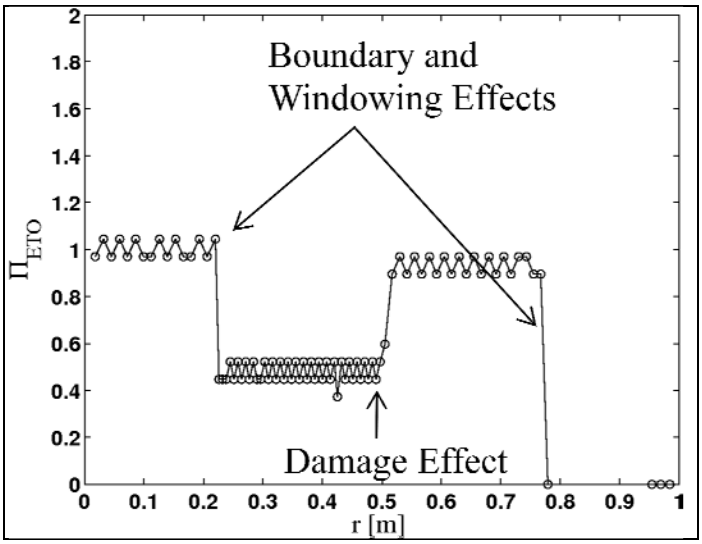

Figure 5. Damage localization parameter, Π_{ETO}, as a function of radial distance.

3.2 Damage Quantification

The mode coefficient formulation is applied to numerical parameterization for the undamaged and damaged configurations using simplified 2-D plane strain, where mode conversion estimation is shown as a function of the fillet radius, excitation frequency, and stiffener cross-sectional thickness (table 1 and figure 6).

Table 1. Test matrix of 2-D FEM parameterization.

Set	Signal	Plate-Stiffener Geometry		Notch Damage Geometry	
	Frequency (kHz)	Fillet Radius (mm)	Stiffener Thickness (mm)	Depth (mm)	Orientation (°)
1	200.0	0.0:3.0:12.0	3.0	—	—
2	200.0	0.0:3.0:12.0	3.0	3.0	0.0
3	200.0	6.0	3.0	0.0:2.0:8.0	0.0
4	200.0	6.0	3.0	3.0	0.0:15.0:75.0

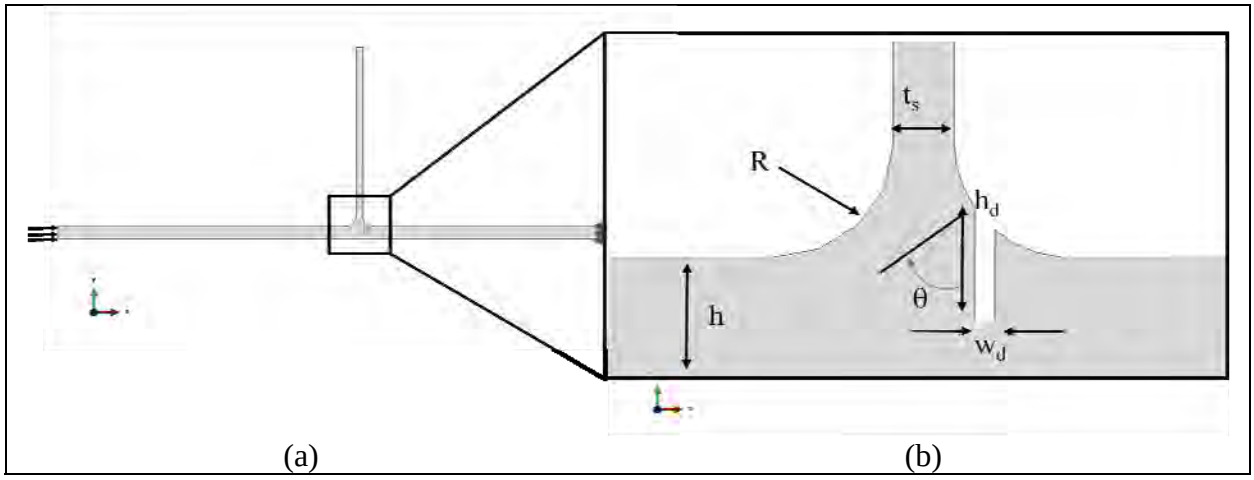

Figure 6. Schematic of 2-D FEM T-joint showing the following: (a) profile with identified boundary conditions and (b) magnified view of FEM parameters at fillet with notch damage.

From figures 7a and b, the mode coefficients from a no-damage configuration vary parabolically as a function of the fillet radius. With a constant damage depth in figure 8a, the R_{So} mode coefficients varies linearly as a function of the fillet radius. As the fillet radius increases (>6 mm), the mode coefficients from undamaged to damaged are approximately equivalent (figure 8b). The thickness of the fillet radius (>6 mm) requires that the damage depth does not penetrate the plate thickness, and sensitivity is negligible. The R_{So} mode coefficient is sensitive to the increasing damage depth, whereas the C_{Ao} mode coefficient shows perturbation (>4 mm) once the damage depth penetrates the plate thickness (figures 9a and b). The R_{So} and C_{Ao} mode coefficients demonstrate a sinusoidal profile with the notch orientation (figures 10a and b).

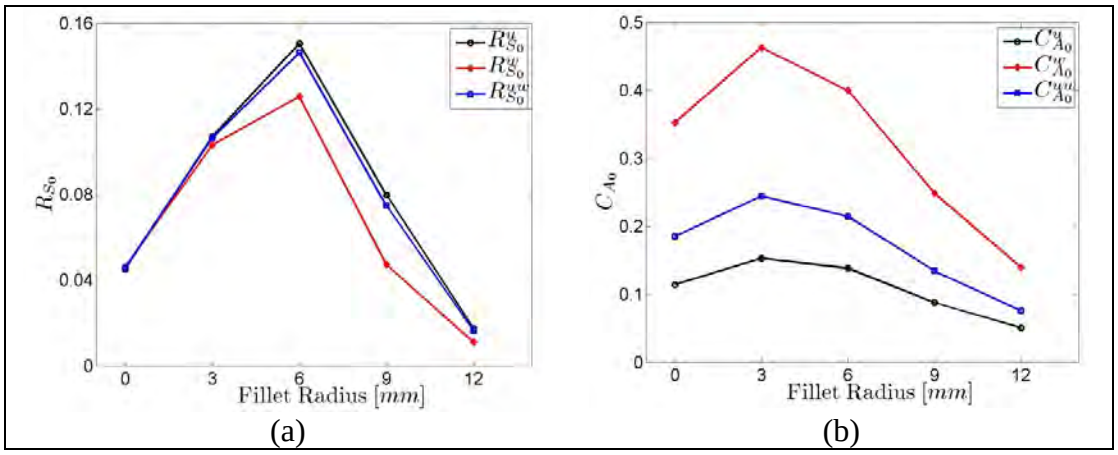

Figure 7. Variation of fillet radius without blind damage showing (a) R_{So} mode coefficient and (b) C_{Ao} mode coefficient.

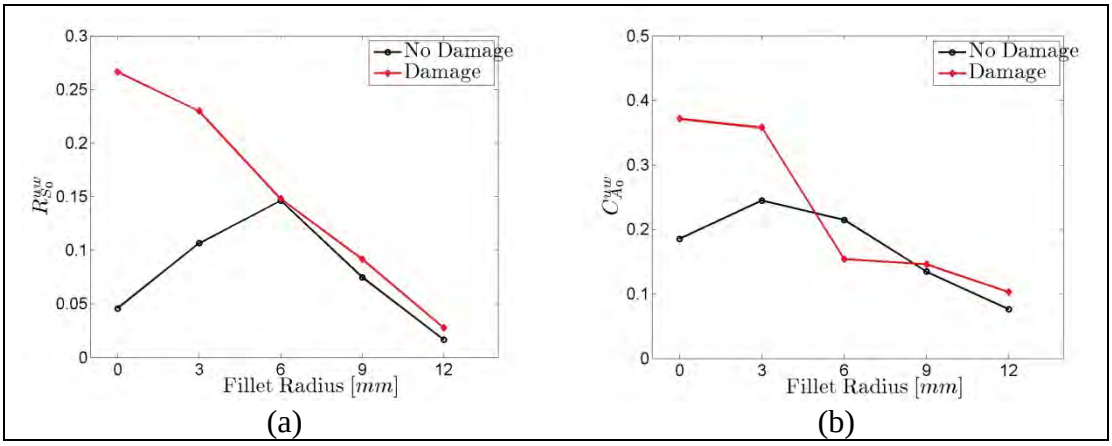

Figure 8. Variation of fillet radius with blind damage of constant depth and orientation showing (a) R_{So} mode coefficient and (b) C_{Ao} mode coefficient.

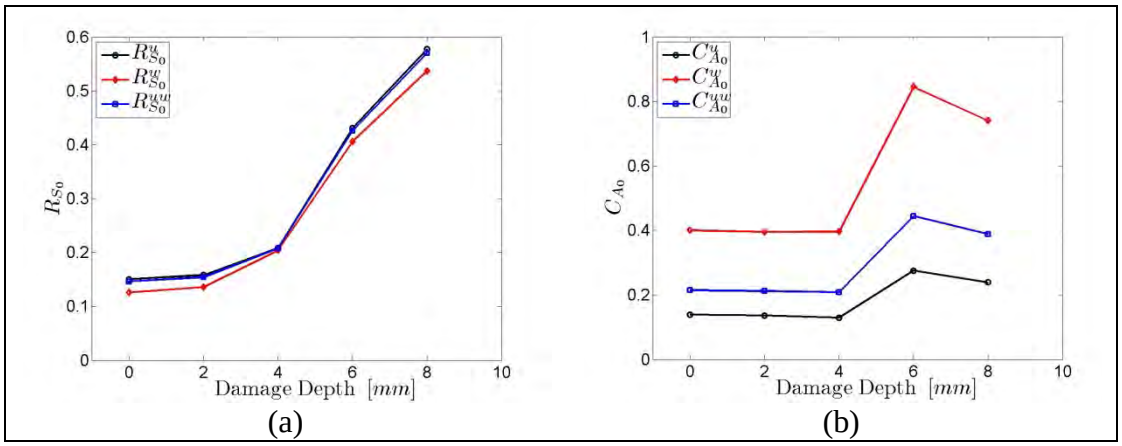

Figure 9. Variation of blind damage depth with constant fillet radius showing (a) R_{So} mode coefficient and (b) C_{Ao} mode coefficient.

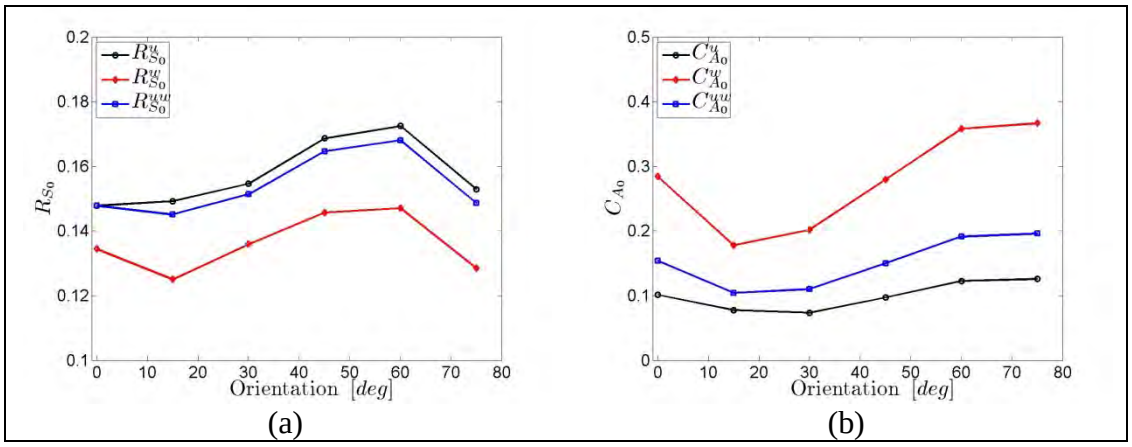

Figure 10. Variation of blind damage orientation with constant fillet radius showing (a) R_{So} mode coefficient and (b) C_{Ao} mode coefficient.

4. Experimental Results

4.1 Damage Localization

The damage localization parameters were experimentally verified by testing homogenous metallic and heterogeneous composite specimens with varying types of induced damage. For this report, one of the experimental results is presented, specifically dynamic excitation of a low-cycle, fatigue-induced crack on a 3.175-mm-thick 6061-T6 aluminum plate cut into a dog-bone shape (figure 11a). A single 6.35-mm-diameter × 0.254-mm-thick PZT transducer was bonded approximately on the longitudinal centerline of plate from the hole (center of hole to center of PZT) using M-Bond 200 adhesive. For the experimental testing, a Hamming-windowed, 5 1/2-cycle sine burst excitation signal was generated using an Agilent 33120A arbitrary waveform generator. This signal was amplified using a Krone-Hite 7500 wideband power amplifier. Data collection was performed using a Polytec PSV-400-3D-M SLDV system designed for full-field vibration measurements at frequencies up to 1 MHz (figure 11b). A dense grid of 200 vertical data points was applied for measuring the wavefield response, with an average resolution of 0.7 mm.

For a given tone burst of 100 kHz, the resulting elliptical orientation is presented in figure 12a. The incident period over the radial distance from 0.02 to 0.04 m consists of incident and reflected S_0 modes, with a converted A_0. The resulting period over the 0.02–0.042-m distance is the summation of the incident and reflected fundamental symmetric mode and an additional transmitted A_0 mode. Applying equation 19, the consequent Π_{ETO} is shown in figure 12b. The approximate rise in slope and effective discontinuity at r = 0.042 m is a clear indication of the mode conversion and identifies the crack presence.

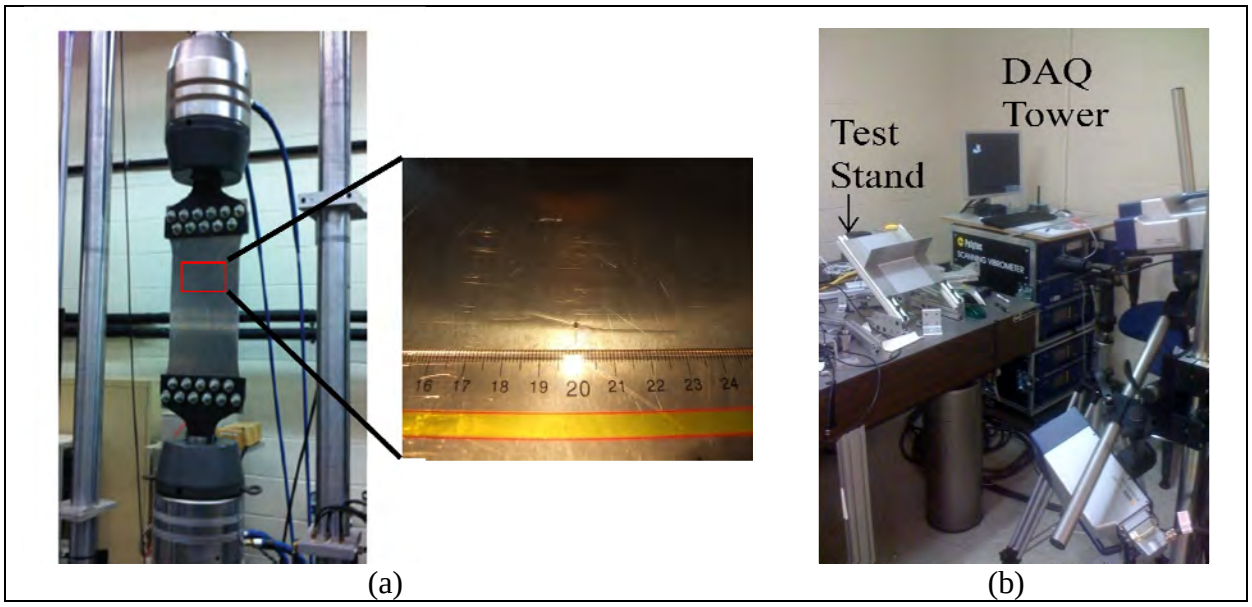

Figure 11. Images showing (a) fatigued aluminum dog bone specimen with 53-mm crack and (b) 3-D SLDV test setup with data acquisition (DAQ) and test stand.

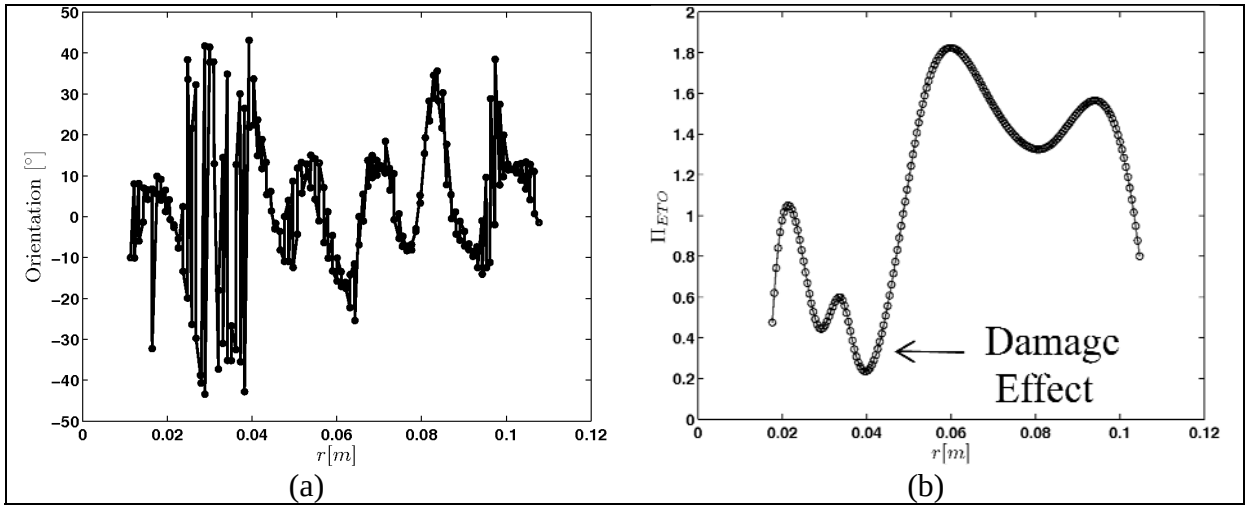

Figure 12. Images showing (a) elliptical orientation of aluminum dog-bone specimen and (b) damage localization parameter, Π_{ETO}, as a function of radial distance.

4.2 Damage Quantification

The trends from the FE parameterization are investigated by using a 3-D scanning laser vibrometry test setup (figure 13a), which consists of an aluminum T-joint for selected fillet radius (0.6 cm), excitation frequency (100 kHz) and stiffener thickness (0.3 cm). The setup enables 3-D surface measurement of the front and back sides of the plate, plate-stiffener radius, and stiffener (figure 13b).

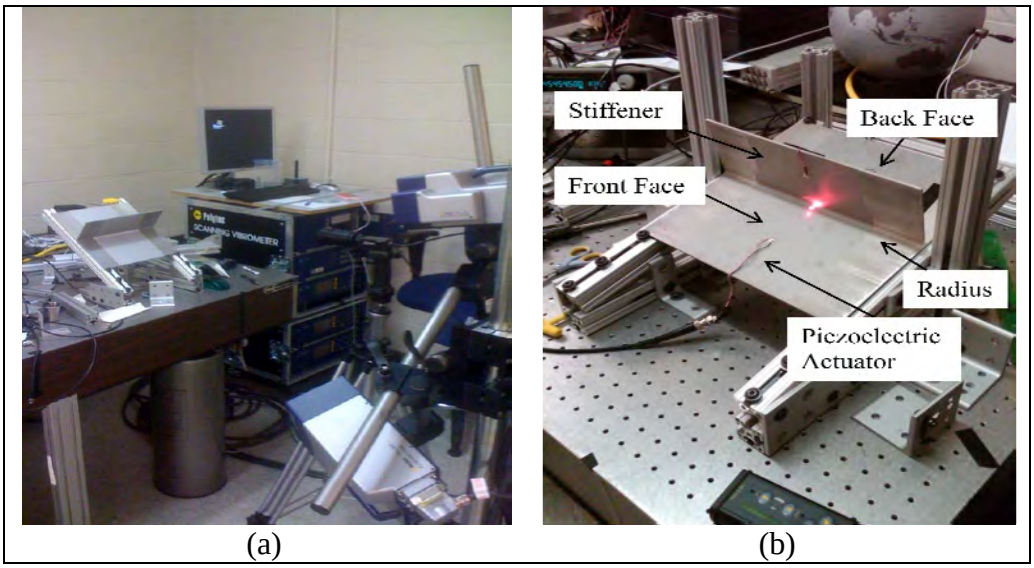

Figure 13. Experimental validation using Polytec 3-D vibrometer showing (a) test setup and (b) aluminum T-joint specimen.

To ensure Lamb wave phenomena, figure 14a illustrates the frequency peaks of the incident A_0 mode of the front face, which aligns with the analytical A_0 mode, while figure 14b shows the back face frequency content, where mode conversion occurs and the S_0 mode is introduced. Figure 15a demonstrates the full wavefield of the filtered out-of-plane A_0 mode along the front face, and figure 15b depicts the in-plane converted S_0 mode. The magnitude of the fillet radius in figure 15b is three orders below that of the front and stiffener surfaces. Using data whose spatial points originate at Y-axis 0.14 m in figure 15a and runs along the front, back, and stiffener faces, table 2 contains the reflection, transmission, and conversion coefficients. Particular attention is given to the difference in order of magnitude between the stiffener and front and back faces, indicating that a significant amount of energy is propagating into the stiffener. The relative order of magnitude, ~0.02–0.06 along the front face for the reflection and conversion mode coefficients, corroborates with the results from the undamaged FE trade studies shown in figure 3.

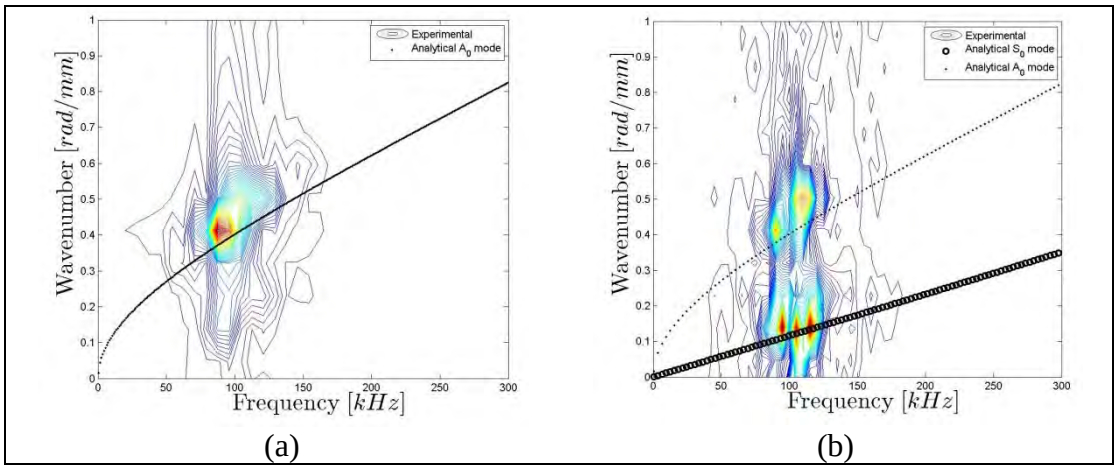

Figure 14. Incident in-plane frequency content showing (a) front face and (b) back face. Excitation frequency of modulated tone burst is 100 kHz.

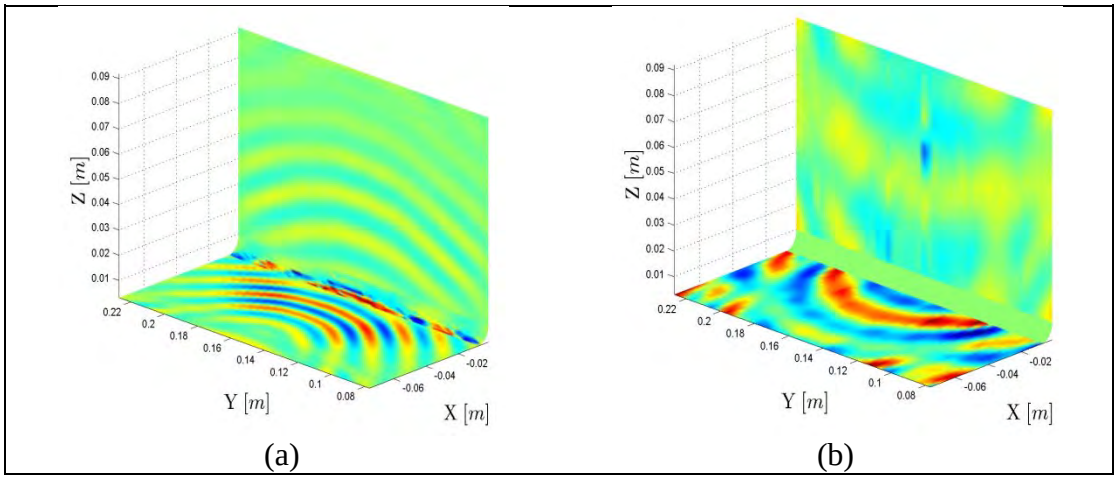

Figure 15. Time history snapshot at 87.8 μs along front face-stiffener surfaces showing (a) filtered incident out-of-plane A_0 mode and (b) filtered converted in-plane S_0 mode.

Table 2. Integrated mode coefficients along center line of three surfaces.

Section	Reflection Coefficients			Transmission Coefficients			Conversion Coefficients		
	R_{A0}^{u}	R_{A0}^{w}	R_{A0}^{uw}	T_{A0}^{u}	T_{A0}^{w}	T_{A0}^{uw}	C_{S0}^{u}	C_{S0}^{w}	C_{S0}^{uw}
Front face	0.054	0.059	0.058	—	—	—	0.053	0.024	0.039
Back face	—	—	—	0.012	0.019	0.017	0.014	0.002	0.009
Stiffener	—	—	—	0.193	0.203	0.199	0.118	0.019	0.074

5. Conclusions

An analytical formulation of the elliptical trajectory is provided, and the technique using the orientation of the elliptical trajectory as a damage localization parameter is investigated on an aluminum specimen with an induced low-cycle fatigue crack. The crack presence was successfully localized, and future work will consist of extending the technique to full damage characterization, which will include damage quantification and complete topology of the damage. In addition, results not presented herein will investigate the damage localization techniques to more complex test specimens that include geometrical complexity and material anisotropy.

In terms of damage quantification, as the fillet radius increases, the mode coefficients from undamaged to damaged are approximately equivalent. The thickness of the fillet radius (>6 mm) does not allow the damage depth to penetrate the plate thickness, and sensitivity to the relative damage is therefore negligible. In addition, the R_{So} and C_{Ao} mode coefficients demonstrate a sinusoidal profile with the notch orientation such that determining the orientation based on the magnitude of the mode coeffiicient is limited. Experimentally, the 3-D laser vibrometry results indicate that the transmission coefficients are an order of magnitude greater within the stiffener section than the front and back faces.

6. References

1. Miklowitz, J. *Theory of Elastic Wave*, North Holland, Holland, 1978, 5–20.
2. Hirao, M.; Fukuoka, H.; Hori, K. *J. of Appl. Mechs*. **1981**, *48*, 119–124.
3. Duquennoy, M.; Ouaftough, M.; Ourak, M. *NDT & E Int.* **1999**, *32*, 189–199.
4. Giurgiutiu, V. *Structural Health Monitoring*; Academic Press: Amsterdam, The Netherlands, 2007.
5. Raghvan, A.; Cesnik, C. *Shock and Vib. Digest* **2007**, *39*, 91–114.
6. Wang, C.; Rose, J. *J. of Sound and Vib.* **2003**, *264*, 851–872.
7. Apetre, N.; Ruzzene, M.; Jacobs, L.; Qu, J. *NDT & E Int.* **2010**, *44*, 247–253.
8. Ayers, J.; Apetre, N.; Ruzzene, M.; Sabra, K. *J Acoust. Soc. Am.* **2011**, *129*, 585–588.
9. Ayers, J.; Apetre, N.; Ruzzene, M. Multiple Component Mode Conversion Coefficients via Lamb Wave Polarization Measurements. In *Proceedings of the SPIE, 7984*; Kundu, T., Ed.; San Diego, CA, 2001; pp 798411–798411-17.
10. Oppenheim, J.; Greve, D. W.; Tyson, N. L. Lamb Wave Behavior in Bridge Girder Geometries. *Proceedings of SPIE, the International Society for Optical Engineering, Smart Structures and Materials*, San Diego, CA, 2006.
11. Ooijevaar, T. H.; Warnet, L. L.; Loendersloot, R.; Akkerman, R.; de Boer, A. Vibration Based Structural Health Monitoring of a Composite Plate Structure With Multiple Stiffeners. *Proceedings of the Fifth European Workshop on Structural Health Monitoring*, Sorrento, Naples, Italy, 2010.
12. Sundaresan, M. J.; Pai, P. F.; Ghoshal, A.; Schulz, M.; Ferguson, F.; Chung, J. F. Methods of Distributed Sensing for Health Monitoring of Composite Material Structures. *Composites: Part A* **2001**, *32*, 1357–1374.
13. Greve, D. W.; Tyson, N.; Oppenheim, I. J. Interaction of Defects With Lamb Waves in Complex Geometries. *IEEE Ultrasonics Symposium* **2005**, 297–300.
14. Morvan, B.; Tine, A.; Duclos, J. Coupling of Lamb Waves at a Tee Junction. *IEEE Ultrasonics Symposium* **1999**, *1*, 565–568.
15. Kim, S.; Lee, C.; Hong, J.; Park, H.; Sohn, H. Applications of an Instantaneous Damage Detection Technique to Plates with Additional Complexities. *J. Nondestructive Evaluation* **2010**, *29*, 189–205.

16. Lanza di Scalea, F.; Matt, H.; Bartoli, I.; Coccia, S.; Park, S.; Farrar, C. Health Monitoring of UAV Wing Skin-To-Spar Joints Using Guided Waves and Macro Fiber Composite Transducers. *J. of Intelligent Material Systems and Structures* **2007**, *18*, 373–388.

17. Kesavan, A.; Deivasigamani, M.; John, S.; Herszberg, I. Damage Detection in T-Joint Composite Structures. *Composite Structures* **2006**, *75*, 313–320.

18. Ruzzene, M. Frequency/Wave Number Filtering for Improved Damage Visualization. *Smart Materials and Structures* **2007**, *16*, 2116–2129.

19. Raghavan, A.; Cesnik, C. *Smart Matls. and Structs*. **2005**, *14*, 1448–1461.

20. Staszewksi, W. J.; Worden, K. Signal Processing for Damage Detection. In *Health Monitoring of Aerospace Structures*; Staszewski, W., Ed.; Wiley & Sons: West Sussex, England, 2004; pp 163–203.

21. Ayers, J.; Apetre, N.; Ruzzene, M. Phase Gradient and Mode Conversion Estimation in 1-D Damaged Structures. *Structural Health Monitoring* **2011**, *1*, 65–82.

22. Moser, F.; Jacobs, L.; Qu, J. *NDTE Int.* **1998**, *32*, 225–234.

NO. OF COPIES	ORGANIZATION
1 (PDF only)	DEFENSE TECHNICAL INFORMATION CTR DTIC OCA 8725 JOHN J KINGMAN RD STE 0944 FORT BELVOIR VA 22060-6218
1	DIRECTOR US ARMY RESEARCH LAB IMNE ALC HRR 2800 POWDER MILL RD ADELPHI MD 20783-1197
1	DIRECTOR US ARMY RESEARCH LAB RDRL CIO LL 2800 POWDER MILL RD ADELPHI MD 20783-1197
1	DIRECTOR US ARMY RESEARCH LAB RDRL CIO MT 2800 POWDER MILL RD ADELPHI MD 20783-1197
1	DIRECTOR US ARMY RESEARCH LAB RDRL D 2800 POWDER MILL RD ADELPHI MD 20783-1197